RSC Advances

PAPER

View Article Online
View Journal | View Issue

Cite this: *RSC Adv.*, 2026, **16**, 12226

Ion transport for simultaneous nickel electrodeposition and sulfuric acid recovery in single-membrane, dual-chamber electrolyzers

Qiaoling Xian,[a] Jian Zhou, *[ab] Hongyi Liu,[a] Chao Guo,[a] Yan Lu[a] and Xinyang Zhou[a]

Received 15th December 2025
Accepted 5th February 2026

DOI: 10.1039/d5ra09684g

rsc.li/rsc-advances

This study introduces an effective single-membrane, dual-cell electrolysis system designed to overcome the limitations of conventional cloth-type membrane bag electrolysis, such as low current efficiency, high energy consumption, and poor product purity. The proposed process enables simultaneous recovery of nickel and sulfuric acid from nickel-rich wastewater. The ion transport behavior is elucidated by comparing the electrolytic performance of five different anion exchange membranes (IONSEP, LanRan, ACM, FAA, and AMV) and analyzing the dynamic changes in ion composition within the anode and cathode chambers. Scanning electron microscopy and X-ray diffraction techniques are employed to characterize the morphological and structural properties of the resulting nickel deposits. The findings reveal that the optimal electrolysis duration is 4 h. Among the tested membranes, the AMV membrane exhibits the best performance, achieving a cathodic current efficiency of 98.5%, energy consumption of 5945.8 kWh per tonne, and anodic sulfuric acid concentration of 38.1 g L^{-1}. The deposited nickel layer displays a smooth, dense, defect-free surface, with continuous and uniform grain growth. The XRD patterns of the nickel coating confirm a distinct preferred orientation along the (220) crystal plane, indicative of high crystallinity and purity. Overall, the single-membrane, dual-cell electrolysis technology improves resource recovery and offers a viable route for treating high-concentration nickel-containing wastewater.

1. Introduction

Nickel, a transition metal of significant industrial value, is widely used in electroplating, battery manufacturing, alloy production, and chemical catalysis due to its excellent corrosion resistance, high mechanical strength, and favorable electrochemical properties.[1–4] However, wastewater from these industrial processes, often containing high concentrations of nickel, presents significant environmental challenges. This wastewater is characterized by complex pollutant profiles, diverse chemical constituents, elevated nickel levels, poor biodegradability, high chromaticity, strong toxicity, and chemical stability.[5,6] Once discharged, it accumulates in aquatic or terrestrial ecosystems, where nickel primarily exists in the form of Ni^{2+}.[7] Due to its high toxicity, poor degradability, solubility, and mobility, nickel readily disperses in the environment, leading to bioaccumulation in the food chain and posing serious safety risks to the water and soil ecosystems.[8,9] Beyond environmental damage, nickel-rich wastewater represents a loss of valuable resources and a threat to human health. Excessive nickel exposure can lead to a range of toxic effects, including contact dermatitis, pulmonary fibrosis, cardiovascular and renal dysfunction, and even carcinogenicity.[10] Therefore, effective treatment of high-concentration nickel-containing wastewater is critical to safeguarding both ecosystems and public health.

The rapid expansion of the energy sector, particularly the continuously increasing demand for nickel in lithium-ion battery cathode materials (*e.g.*, ternary materials), has intensified research into efficient nickel recovery and recycling technologies.[11,12] Conventional methods, including chemical precipitation,[13] solvent extraction,[14] and adsorption,[15,16] primarily alter the chemical form of Ni^{2+} without eliminating its environmental hazards. These approaches often involve complex operations, high energy consumption, and secondary pollution, limiting their suitability for modern sustainable manufacturing and resource recovery goals.[17,18] For example, chemical precipitation generates large volumes of nickel-containing sludge. Tamersit *et al.*[19] demonstrated that coupling Donnan dialysis with precipitation enables selective nickel recovery from electroplating rinse bath wastewater, highlighting the superior performance of membrane-based processes in low-concentration systems. By contrast, solvent extraction and adsorption heavily rely on organic reagents or engineered materials, increasing environmental burdens and complicating post-treatment management.

[a]*School of Environmental and Municipal Engineering, Lanzhou Jiaotong University, Lanzhou 730070, China. E-mail: zhoujian@lzjtu.edu.cn*

[b]*Ministry of Education Engineering Research Center of Water Resource Comprehensive Utilization in Cold and Arid Regions, Lanzhou 730070, China*

Electrolytic extraction of metallic nickel[20] is typically conducted in chloride- or sulfate-based systems,[21,22] depending on the electrolyte composition. Chloride systems generally offer better conductivity, lower cell voltage, and reduced energy consumption than sulfate systems. However, the volatility of hydrochloric acid and the production of chlorine gas at the anode during electrolysis raise serious environmental concerns. Consequently, $NiSO_4$-based electrolytes are now widely employed in both domestic and international operations.[23] The conventional nickel sulfate electrolysis process employs cloth-type membrane bags to separate the anode and cathode chambers. However, due to the insufficient electrolyte separation of electrolytes between the two electrodes, protons (H^+) generated at the anode migrate to the cathode, where they compete with Ni^{2+} ions for reduction. This competition reduces nickel deposition quality, promotes hydrogen evolution, decreases current efficiency, and increases overall energy consumption.[24]

To address these limitations, this study employs a single-membrane, dual-cell electrolytic cell system in which the traditional physical diaphragm is replaced with an anion exchange membrane (AEM). This configuration effectively separates the anolyte and catholyte, suppresses H^+ migration, and significantly enhances both nickel deposition efficiency and product purity. Simultaneously, sulfuric acid is enriched in the anode chamber, enabling synchronous nickel recovery.[25,26] This integrated approach combines the advantages of resource recycling and process intensification, offering a sustainable pathway for the treatment of high-concentration nickel-containing wastewater.

Previous studies support the advantages of membrane electrolysis. For instance, Rögener *et al.*[27] demonstrated nickel recovery from pickling wastewater, showing that both the metal deposition rate and current efficiency increased with current density. Loza *et al.*[28] compared different ion-exchange membranes for the separation of $H_2SO_4/NiSO_4$ *via* diffusion dialysis, finding that strongly basic AEMs effectively decoupled sulfuric acid from nickel sulfate, whereas cation exchange membranes (CEMs) failed to achieve efficient separation. Yan *et al.*[29] integrated two-chamber electrodeposition with electrodialysis for the treatment of spent electroless nickel plating baths, achieving simultaneous Ni^{2+} recovery and phosphate anion removal, further highlighting the potential of membrane electrolysis for combined separation, enrichment, and deposition.

In this study, membrane electrolysis is performed using a single-membrane, dual-cell electrolytic cell for nickel electrodeposition from a nickel sulfate electrolyte. Simultaneously, sulfuric acid is enriched and recovered in the anode chamber, enabling highly efficient resource recycling. The dynamic changes in ionic composition within both the anolyte and catholyte are monitored throughout electrolysis, and the ion transport behavior is investigated to evaluate the feasibility of the proposed technology. Additionally, the electrolytic performance of five different AEMs is systematically compared, offering a reference framework for boosting the industrial applications of this technology.

2. Materials and methods

2.1 Experimental materials

Five different types of AEMs were evaluated: a Chinese heterogeneous membrane (IONSEP-AIM), a Chinese homogeneous membrane (LanRan-ACE), a Japanese homogeneous membrane (ACM A-0198), a German homogeneous membrane (FAA-3PK-75), and an American homogeneous membrane (AMV). Their performance parameters are summarized in Table 1.

Simulated wastewater was prepared in the laboratory based on the concentration profiles of actual nickel-rich wastewater from the Jinchuan Nickel Smelter. The catholyte was formulated using nickel sulfate hexahydrate (analytical grade, ≥98.0%) and boric acid (analytical grade, ≥99.5%), yielding a nickel ion concentration of 40 g L^{-1} and a boric acid concentration of 20 g L^{-1}. Sodium dodecyl sulfate (SDS, chemically pure) was added as an additive at a concentration of 0.05 g L^{-1}. The anolyte consisted of a 0.05 mol L^{-1} dilute sulfuric acid solution prepared from concentrated sulfuric acid (analytical grade, 98.0%). All chemical reagents were supplied by Shanghai McLean Biochemical Technology Co., Ltd, China.

2.2 Experimental device

Electrodeposition experiments were conducted using a custom-designed single-membrane, dual-cell electrolytic system, as illustrated in Fig. 1. This apparatus employs an AEM to separate the anode and cathode chambers. Each chamber has an effective volume of 225 mL and features a symmetrical design with identical geometric dimensions.

Both chambers were equipped with independent electrolyte circulation systems, with flow rates controlled by peristaltic pumps. The anode was a titanium-based iridium–ruthenium plate (15 cm × 8 cm), while the cathode was constructed from corrosion-resistant stainless steel (15 cm × 7 cm). The internal support frames and external mounting brackets were fabricated

Table 1 Performance parameters of the ion exchange membranes used in this study

Membrane	Thickness (mm)	Exchange capacity (mmol g^{-1})	Resistance (Ω cm^2)	Permselectivity (%)
IONSEP-AIM	0.38–0.42	>1.6	≤15	>90
LanRan-ACE	0.22	1.4	4	96
ACM A-0198	0.11–0.15	1.5–2.0	≤3.0	≥90
FAA-3PK-75	0.07–0.08	1.2–1.4	1.2–2.0	95
AMV	0.12	2.0	2.5	≥96

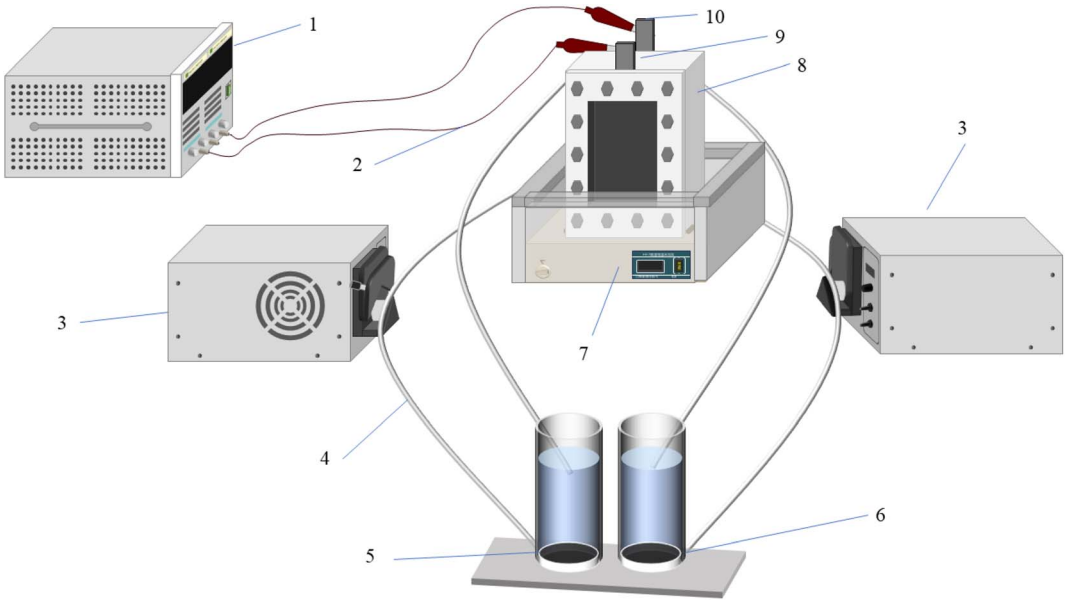

Fig. 1 Schematic diagram of experimental device: (1) constant-voltage constant-current DC power supply; (2) wire; (3) peristaltic pump; (4) silicone tubing; (5) anode circulation tank; (6) cathode circulation tank; (7) digital thermostat water bath; (8) single-membrane, dual-cell electrolyzer; (9) anode plate; (10) cathode plate.

from acrylic glass to ensure structural stability and chemical resistance. To maintain airtight sealing, elastic silicone seals were installed at all connection interfaces. The entire assembly was secured with chemically resistant fastening bolts, resulting in fully sealed and independent reaction chambers.

2.3 Data processing

(1) Current efficiency:

$$\eta_A = \frac{m_A}{q_A I t} \times 100\% \quad (1)$$

where η_A is the cathodic current efficiency for nickel deposition (%); m_A is the mass of nickel deposit (g); I is the current (A); t is the electrolysis duration (h); q_A is the electrolytic equivalent of nickel, taken as 1.095 g $(Ah)^{-1}$.

(2) Sulfuric acid generation:

$$C = C_2 - C_1 \quad (2)$$

where C is the increase in sulfuric acid concentration (g L^{-1}); C_1 and C_2 are the sulfuric acid concentrations before and after electrolysis (g L^{-1}).

(3) Electrical energy consumption:

$$W_A = \frac{U \times 1000}{q_A \times \eta_A} \quad (3)$$

where W_A is the specific energy consumption for nickel electrodeposition (kWh per tonne); U is the applied cell voltage (V).

2.4 Analytical methods

H^+ concentration was determined by titration with sodium hydroxide using phenolphthalein as the indicator. Ni^{2+} concentration was measured by flame atomic absorption spectrophotometry. SO_4^{2-} concentration was determined *via* barium chromate spectrophotometry. The solution pH was measured using a PHS-3C precision pH meter, calibrated with standard buffer solutions to ensure accuracy.[30]

The surface morphology was examined by scanning electron microscopy (SEM) coupled with energy-dispersive X-ray spectroscopy (EDS) using a ZEISS GeminiSEM 500 system (Germany). The crystal structure of the electrode surface was analyzed by X-ray diffraction (XRD) over a scanning range of 30°–80°.

2.5 Experimental procedures

The AEM was pretreated by immersion in either deionized water or a 0.5 mol L^{-1} NaCl solution for 24 h prior to use. Working electrodes were polished to a mirror finish, ultrasonically cleaned with deionized water to remove residual particles, and insulated on the reverse side with tape. The polishing and cleaning steps were repeated after each experiment to ensure surface consistency.

For each experimental run, 500 mL of anolyte and catholyte solutions were prepared, with a 30 mm electrode spacing. The temperature was controlled at 35 ± 1 °C using a constant-temperature digital water bath. The electrolyte circulation rate in both electrode chambers was controlled at 0.06 m s^{-1} using a peristaltic pump. Electrolysis was performed under a constant current mode at a current density of 350 A m^{-2}. Throughout the process, the cell voltage was continuously monitored, and electrolyte samples were periodically collected for analysis.

After electrolysis, the deposited nickel layer was weighed using an electronic balance. The nickel foil was then carefully

peeled from the electrode surface and collected for subsequent purity analysis.

3. Results and discussion

3.1 Nickel electrodeposition using different AEMs

Fig. 2 illustrates the impact of five different AEMs on nickel electrodeposition in a single-membrane, dual-chamber electrolytic cell over varying electrolysis durations.

As depicted in Fig. 2(a), the cell voltage gradually increases with electrolysis time. Among the tested membranes, the FAA membrane maintains the lowest cell voltage. This gradual rise in cell voltage is primarily attributed to the declining concentration of active ions in the electrolyte, which reduces conductivity and necessitates a higher driving voltage to sustain the electrochemical reaction. The FAA membrane, with the lowest resistance, consistently exhibits superior performance, whereas the IONSEP-AIM membrane, with the highest resistance, shows significantly higher cell voltage than the other four membranes. The higher cell voltage observed in the single-membrane, dual-chamber electrolysis system compared to conventional undivided cells is largely due to the presence of the AEM, which introduces concentration polarization overpotential at the membrane–solution interface.[30] Nevertheless, this increase remains acceptable from both technical and economic perspectives.

Fig. 2(c) and (d) demonstrate that both sulfuric acid generation and energy consumption increase with electrolysis time. After 6 h, the AMV membrane achieves the highest acid recovery, raising the sulfuric acid concentration in the anode

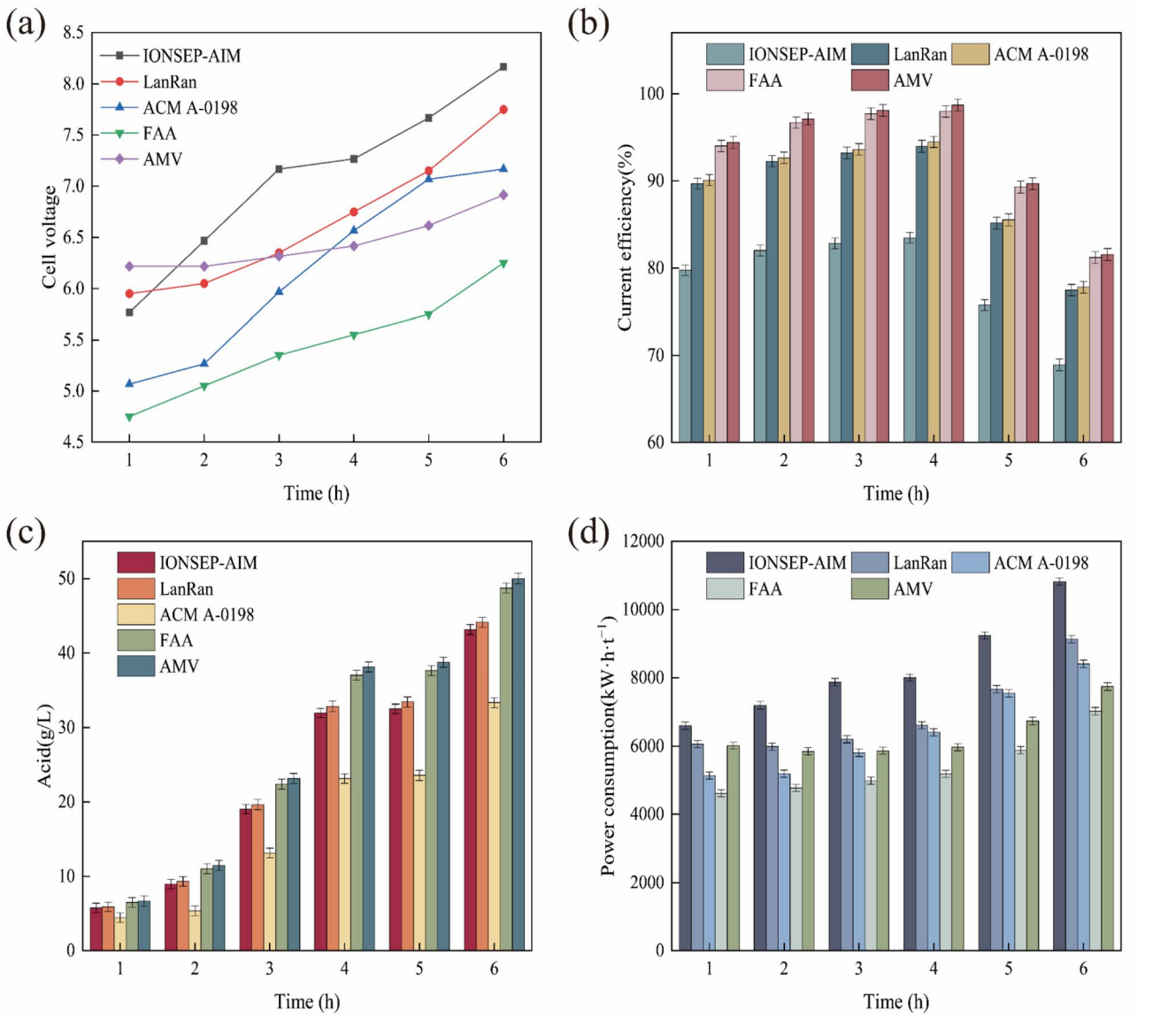

Fig. 2 (a) Variation in the cell voltage over time for different anion exchange membranes (AEMs); (b) effect of different AEMs on current efficiency; (c) effect of different AEMs on sulfuric acid generation; (d) effect of different AEMs on energy consumption.

chamber from 0.05 mol L^{-1} to approximately 0.5 mol L^{-1}, followed by the FAA membrane. Despite its lower acid recovery, the FAA membrane exhibits the lowest energy consumption, with the AMV membrane closely following. Since the current density remains constant, the overall rise in energy consumption is primarily driven by the increase in cell voltage. This voltage increase results from two factors: (i) the competition between H^+ and Ni^{2+} for reduction, which compromises nickel deposition purity and increases energy demand, and (ii) the continuous decline in Ni^{2+} concentration, which increases system resistance and further amplifies energy consumption.[31]

Fig. 2(b) illustrates that the current efficiency for all five membranes initially increases with electrolysis time, reaching a maximum at 4 h, before gradually declining. During the first 4 h, electrode surfaces are fully activated, mass transfer conditions are optimized, and the electrolyte system attains a steady state. Under these conditions, the diffusion rates of reactants and products are balanced. However, prolonged electrolysis leads to concentration polarization and intensified side reactions, particularly hydrogen evolution reaction (HER), which reduce nickel deposition efficiency.[32]

The AMV membrane demonstrates the best overall performance due to its ultra-thin and compact polymer network, high ion exchange capacity (2.0 mmol g^{-1}), and excellent anion selective permeability (up to 96%). These properties significantly enhance SO_4^{2-} transmembrane migration.[33] Although the FAA membrane has a similar thickness, its cross-linked structure yields lower resistance and consequently the lowest cell voltage. According to the principle of electroneutrality, SO_4^{2-} ions migrating into the anode chamber combine with H^+ to form H_2SO_4. This mechanism explains the superior acid recovery achieved by the AMV membrane, effectively enabling sulfuric acid enrichment and resource recycling.[34]

Furthermore, during the electrochemical deposition process, the cathodic reduction of Ni^{2+} is primarily governed by the concentration gradient within the diffusion layer. The dual-chamber design of the electrolytic system prevents interference from anodic oxidation products at the cathode, further enhancing current efficiency.[35]

In summary, after 6 h of electrolysis, the electrodeposition efficiencies of IONSEP-AIM and LanRan-ACE were lower than those of ACM A-0198, FAA-3PK-75, and AMV membranes. With increasing electrolysis time, the cell voltage rose continuously, accompanied by a gradual increase in energy consumption. The current efficiency initially improved, peaking at ~4 h, before declining. Among the tested AEMs, the AMV membrane exhibited the best overall electrochemical performance, achieving a current efficiency of 98.5%, sulfuric acid concentration of 38.1 g L^{-1}, and energy consumption as low as 5945.8 kWh per tonne. Based on a balance of economic efficiency and energy conservation, an electrolysis duration of 4 h is identified as the optimal condition for nickel electrodeposition.

3.2 Product characterization under optimal membrane conditions

Fig. 3 presents the surface morphology and elemental composition of the cathodic nickel deposits obtained after 4 h of electrolysis using the AMV membrane. SEM images at 500× (Fig. 3(a)) and 2000× magnifications (Fig. 3(b)) reveal dense nickel deposits with relatively large particle sizes. No obvious defects such as cracks, pores, or particle agglomeration are observed, indicating a continuous and uniform growth process.[36,37] At higher magnification (Fig. 3(b)), the crystal surfaces exhibit a pyramid-like morphology, consistent with the spiral dislocation growth mechanism, suggesting that the

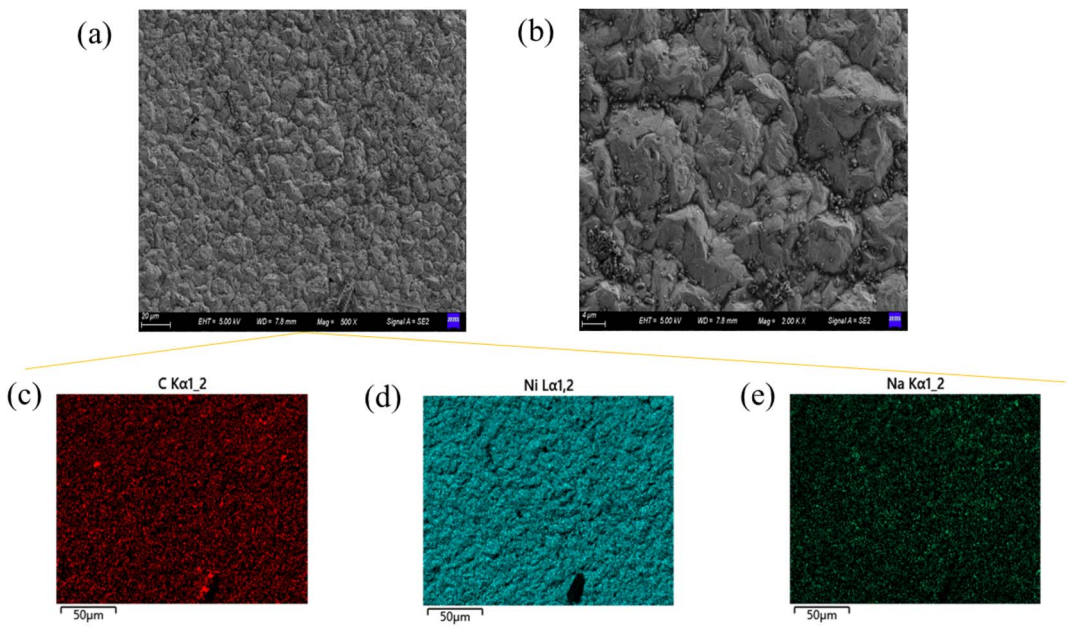

Fig. 3 SEM images of cathodic nickel deposits obtained under the AMV membrane: (a) 500× magnification; (b) 2000× magnification. (c) C spectrum; (d) Ni spectrum; (e) Na spectrum.

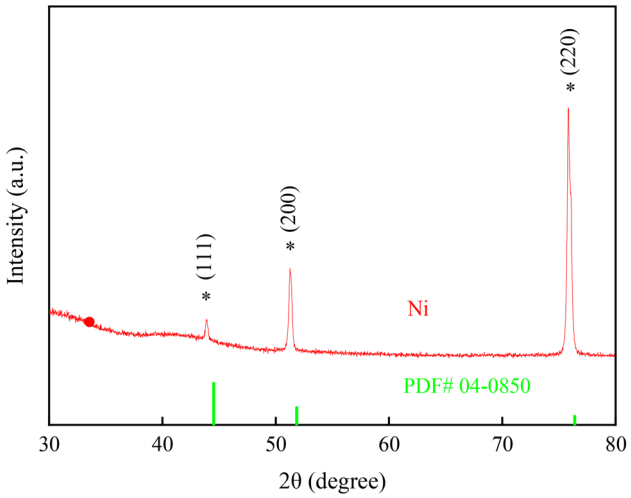

Fig. 4 XRD pattern of cathodic products obtained under AMV membrane conditions.

deposition process is primarily governed by dislocation-driven layered growth rather than instantaneous nucleation.[38,39]

EDS analysis confirms the presence of nickel in the coating, along with carbon and sodium signals attributed to the adsorption and incorporation of the SDS additive during electrodeposition. The presence of trace sodium ions within the deposit is known to promote nickel ion reduction and improve coating quality.[40–42]

The crystallinity of the nickel deposits was evaluated by XRD analysis. As shown in Fig. 4, the cathodic product exhibits diffraction peaks at 2θ values of 43.9°, 51.3°, and 75.8°. Compared with the standard PDF card for face-centered cubic (FCC) nickel (no. 04-0850), these peaks display slight shifts from the reference positions: (111) plane at 44.5°, (200) plane near 51.8°, and (220) plane near 76.4°. Such minor displacements may be attributed to lattice distortions caused by the adsorption or incorporation of the additive during electrodeposition, which alters the interplanar spacing. Additionally, residual stresses within the nickel coating can slightly modify the lattice parameters, contributing to these small deviations. Notably, the peak shifts are minimal, and no extraneous peaks are observed, confirming the preservation of the FCC crystal structure and high purity of the nickel deposits.[43]

The weak adsorption of SDS molecules on the cathode surface regulates the mass transfer boundary layer in the near-electrode region. This promotes uniform Ni^{2+} distribution at the interface, reduces local concentration polarization, and suppresses irregular or dendritic growth, thereby favoring the stable growth of low-surface-energy crystal planes.[44]

In a randomly oriented, unstressed nickel sample, the (111) peak typically exhibits the highest intensity, followed by the (200) and (220) peaks, with an intensity ratio of approximately 100 : 42 : 21. However, as shown in Fig. 4, the (220) peak is the most intense, indicating a preferred grain orientation along the (220) plane. According to geometric selection theory, during electrodeposition, the growth-restricted (220) plane is gradually preserved as faster-growing planes cover the surrounding regions. This process ultimately results in the deposited layer being dominated by the (220)-oriented grains.[36] Consequently, the proportion of (220)-oriented grains in the nickel deposit significantly increases, reflecting pronounced preferential orientation during the late stage of electrocrystallization.[45] This finding is consistent with the regular crystallographic plane morphology observed in SEM, confirming that the additive primarily regulates crystal growth kinetics to achieve selective surface growth. Importantly, this regulation does not compromise the crystal structure or purity of the nickel product.[46]

3.3 Ion transport behavior during nickel electrodeposition

The theoretical foundation of single-membrane, dual-chamber electrolysis lies in the coupling between the selective transport properties of ion-exchange membranes and the electrochemical deposition process. This method leverages the selective permeability of ion-exchange membranes, combined with the migration of charged ions under a direct current (DC) electric field, to achieve coordinated separation and enrichment of target species.[41] During membrane electrolysis, the electric field serves as primary driving force, simultaneously inducing electrochemical and concentration polarization within the cell. Consequently, ion migration, diffusion, and electroosmotic transport become the dominant mechanisms governing the electrolytic reaction.[42]

In this system, an AEM divides the conventional electrolytic cell into separate cathode and anode chambers. The ion transport processes between the electrolytes in these two chambers are schematically illustrated in Fig. 5. Under an applied current electric field, Ni^{2+} ions migrate toward the cathode, where they are reduced to metallic nickel. Concurrently, HER may occur as a side reaction. Meanwhile, SO_4^{2-} ions selectively migrate through the AEM into the anode chamber. Water electrolysis in the anode chamber generates H^+ and O_2 gas.[43] Due to the selective blocking function of the AEM, H^+ ions are effectively confined to the anode chamber and prevented from entering the cathode chamber. This confinement stabilizes the catholyte pH and significantly suppresses the side reaction (*i.e.*, HER), thereby improving both the efficiency and quality of nickel electrodeposition.

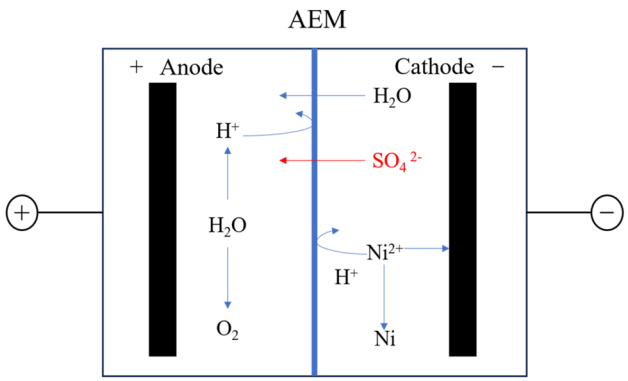

Fig. 5 Schematic diagram of ion transport in single-membrane, dual-chamber electrolytic cell during nickel sulfate electrowinning.

Similarly, Ni^{2+} ions in the catholyte are retained within the cathode chamber due to the combined effects of repulsion from the anode electric field and physical blocking by the AEM. Maintaining a high Ni^{2+} concentration minimizes concentration polarization, facilitating nickel deposition, improving current efficiency, and ensuring that the ionic conductivity between the catholyte and anolyte is primarily governed by SO_4^{2-} migration. As electrolysis proceeds, SO_4^{2-} ions continuously migrate from the cathode chamber through the AEM into the anode chamber, where they combine with H^+ ions generated by water electrolysis to form an increasingly concentrated sulfuric acid solution. Once the sulfuric acid concentration reaches a sufficient level, it can be recovered and recycled for use in hydrometallurgical acid leaching or for adjusting catholyte acidity during electrolysis.

The specific electrochemical reactions occurring in the system are as follows:[47]

Cathode reactions:

$$Ni^{2+} + 2e^- \rightarrow Ni \quad (4)$$

$$2H^+ + 2e^- \rightarrow H_2\uparrow \quad (5)$$

Anode reactions:

$$2H_2O - 4e^- \rightarrow 4H^+ + O_2\uparrow \quad (6)$$

$$2H^+ + SO_4^{2-} \rightarrow H_2SO_4 \quad (7)$$

The ion transport behaviors described above can be verified by monitoring the temporal changes in ion concentrations (Ni^{2+}, SO_4^{2-}, H^+) in both the cathode and anode chambers.

3.3.1 Variations in catholyte composition. As shown in Fig. 6, the Ni^{2+} concentration in the catholyte steadily decreases over time under the influence of all five AEMs. This reduction is primarily ascribed to cathodic nickel deposition, where Ni^{2+} are reduced to metallic nickel on the cathode surface.

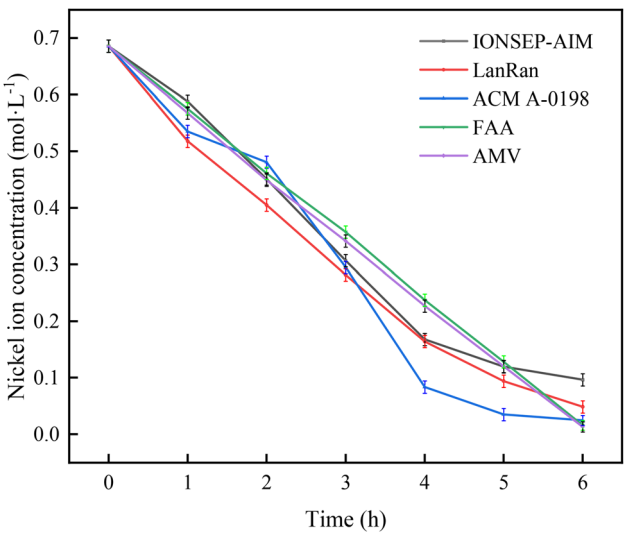

Fig. 6 Variation in Ni^{2+} concentration in the catholyte over time.

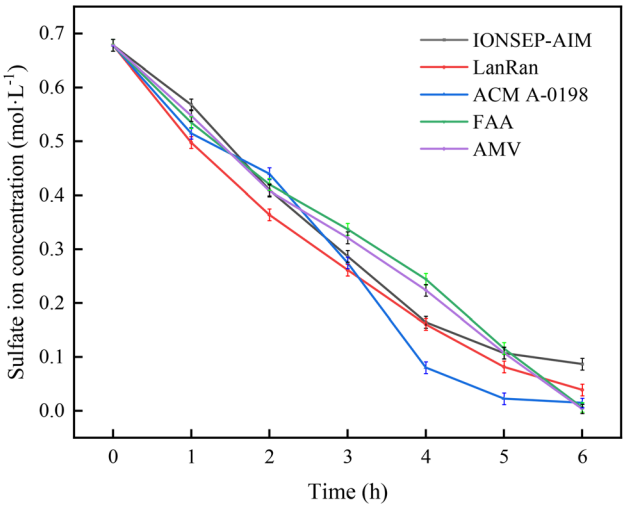

Fig. 7 Variation in SO_4^{2-} concentration in the catholyte over time.

Simultaneously, SO_4^{2-} ions migrate toward the anode chamber under the applied electric field to maintain charge neutrality.[30] Additionally, a small amount of Ni^{2+} ions migrate into the anolyte during electrolysis.

Fig. 7 illustrates that the concentration of SO_4^{2-} ions in the catholyte also decreases continuously over time. This decline occurs because as nickel deposits, SO_4^{2-} ions migrate through the AEM into the anode chamber under the applied electric field, where they combine with H^+ ions generated by water electrolysis to maintain charge neutrality in the catholyte. The variation trends of SO_4^{2-} and Ni^{2+} concentrations over time are similar, with comparable decline rates.

This selective transport behavior is explained by the Donnan exclusion effect of the AEM, which facilitates anion (SO_4^{2-}) migration while effectively blocking cations (Ni^{2+}).[48] However, the rate of decline and final ion concentrations vary among the membranes, reflecting differences in selective permeability determined by their chemical composition and structural design. For instance, the ACM A-0198 membrane shows a rapid decline in ionic concentrations during the first four hours, indicating strong promotion of SO_4^{2-} migration and efficient nickel electrodeposition. Conversely, membranes such as IONSEP-AIM and LanRan demonstrate gradual decline in ion concentration, suggesting relatively stable and moderate ion transport rates.

Overall, these variations in membrane performance highlight differences in the mass transfer efficiency of SO_4^{2-} and Ni^{2+} during electrodeposition within the single-AEM, dual-chamber electrolytic cells.

Fig. 8 shows that the pH of the catholyte gradually decreases with increasing electrolysis time, indicating a continuous rise in acidity within the cathodic region. In the presence of boric acid, the solution maintains a relatively low pH, facilitating the formation of a weak nickel borate complex, $Ni(H_2BO_3)_2$. This complex acts as a homogeneous catalyst, lowering the overpotential required for nickel deposition.[23,49]

Under the applied electric field, a large number of H^+ ions accumulate on the anode side of the AEM. Due to the combined

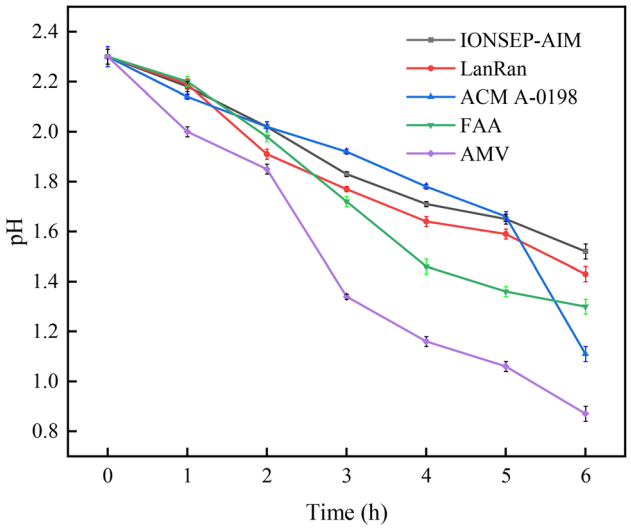

Fig. 8 Variation in catholyte pH over time.

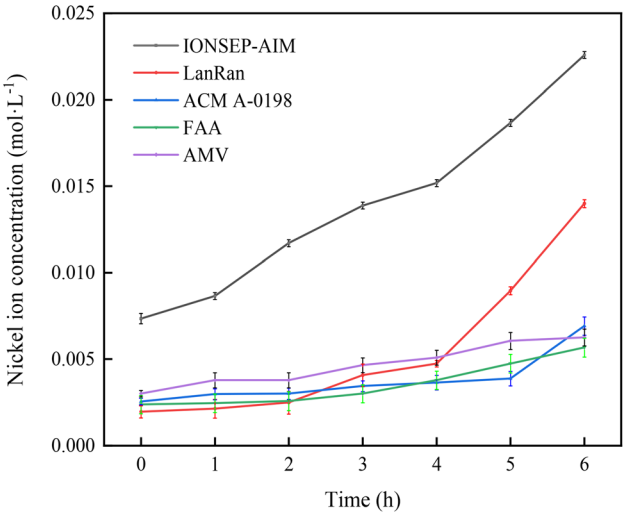

Fig. 10 Variation in Ni^{2+} concentration in the anolyte over time.

effects of the applied electric field and Donnan dialysis, H^+ ions tend to migrate from the anolyte to the catholyte, increasing H^+ adsorption on the membrane surface. However, since the selective permeability of the AEM cannot reach 100%, some H^+ ions diffuse through the membrane into the cathode chamber, driven by the concentration gradient. This diffusion accounts for the observed decrease in the catholyte pH.[46]

When the pH in the cathode chamber reaches a critical threshold, the concentration gradient of H^+ between the anode and cathode sides decreases, reducing the migration rate. Eventually, a dynamic equilibrium is established with the HER at the cathode, causing the pH to stabilize.[50]

3.3.2 Variations in anolyte composition. The AEM effectively separates the anode and cathode chambers through selective permeation, allowing anions (SO_4^{2-}) to pass while blocking cation migration, thereby maintaining charge balance between the two chambers. As shown in Fig. 9, the SO_4^{2-} concentration in the anolyte increases steadily, with a rapid rise during the first four hours, followed by a slower increase. This trend, consistent across all five membranes, results from the synergistic effect of the AEM's selective permeability and the electric field, which promotes directional migration of SO_4^{2-} ions from the cathode to the anode.

Fig. 10 shows that the Ni^{2+} concentration in the anode chamber gradually increases during electrolysis but remains relatively low overall. In the absence of an electric field, Ni^{2+} ions migrate to the anode chamber, mainly by diffusion along their concentration gradient. Meanwhile, at the cathode, Ni^{2+} ions readily form stable complexes with borate ions (such as $H_2BO_3^-$), which further suppresses Ni^{2+} accumulation in the anode chamber.[51]

As shown in Fig. 11, the H^+ concentration in the anode chamber steadily increases during electrolysis, reflecting the ion selectivity of the AEM. Among the membranes tested, the ACM A-0198 membrane exhibits the lowest sulfuric acid recovery, indicating the highest level of H^+ leakage. In the anode

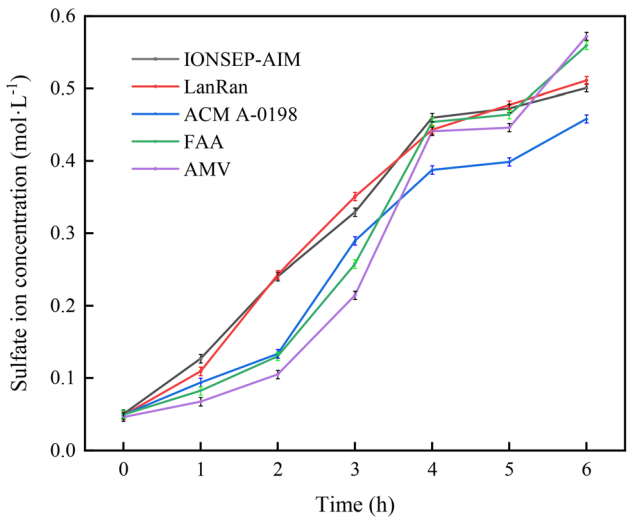

Fig. 9 Variation in SO_4^{2-} concentration in the anolyte over time.

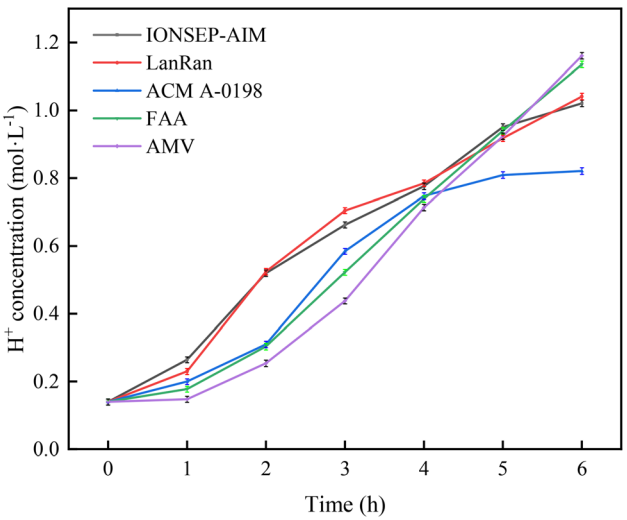

Fig. 11 Variation in H^+ concentration in the anolyte over time.

chamber, H^+ ions are primarily generated by the oxygen evolution reaction (OER), and their production rate far exceeds the H^+ migration rate driven by the electric field.[52]

Due to the cation-blocking properties of the AEM, H^+ ions cannot migrate to the cathode and thus accumulate in the anode chamber. These H^+ ions combine with SO_4^{2-} migrating from the catholyte to form H_2SO_4.[53] The increase in H^+ concentration in the anolyte is governed by both diffusion and electromigration, driven by the H^+ concentration gradient and the applied electric field, respectively. The combined action of these mechanisms results in the progressive accumulation of H^+ ions in the anode chamber, with its fundamental source being the continuous H^+ generation *via* OER. Furthermore, the relatively high sulfuric acid recovery observed with the FAA membrane may be attributed to its highly cross-linked or hydrophobic backbone, which reduces H^+ permeability.[54]

3.4 Ion transport characteristics

The flux of each ion in the electrolyte can be described by the Nernst–Planck equation,[55] which characterizes ion transport through ion-exchange membranes or between the diffusion boundary layer and the bulk solution, as shown in eqn (8). The ion flux is governed by three driving forces: diffusion due to concentration gradients, migration under potential gradients, and convection resulting from fluid flow perpendicular to the membrane.[56]

$$J_i = -D_i \nabla c_i - z_i u_{\mathrm{mob},i} F c_i \nabla \varphi_i + c_i \vec{v} \tag{8}$$

The first term on the right represents diffusion, where D_i is the diffusion coefficient ($m^2\ s^{-1}$), and c_i is the ion concentration. The second term corresponds to migration, where z_i is the ion charge, $u_{\mathrm{mob},i}$ is the ion mobility (s mol kg^{-1}), $F = 96\,485$ C mol^{-1} is the Faraday's constant, and φ_i is the electrolyte potential. The third term accounts for convection, where $\vec{v}$ denotes the fluid velocity vector ($m\ s^{-1}$).

Within the electrode chamber, ions migrate and transfer mass according to these mechanisms. By simplifying eqn (8), the ion flux can be expressed as follows:[57]

$$J_i = -D_i \frac{\Delta c_i}{\delta_m} + \frac{t_i I}{z_i F} + c_i v \tag{9}$$

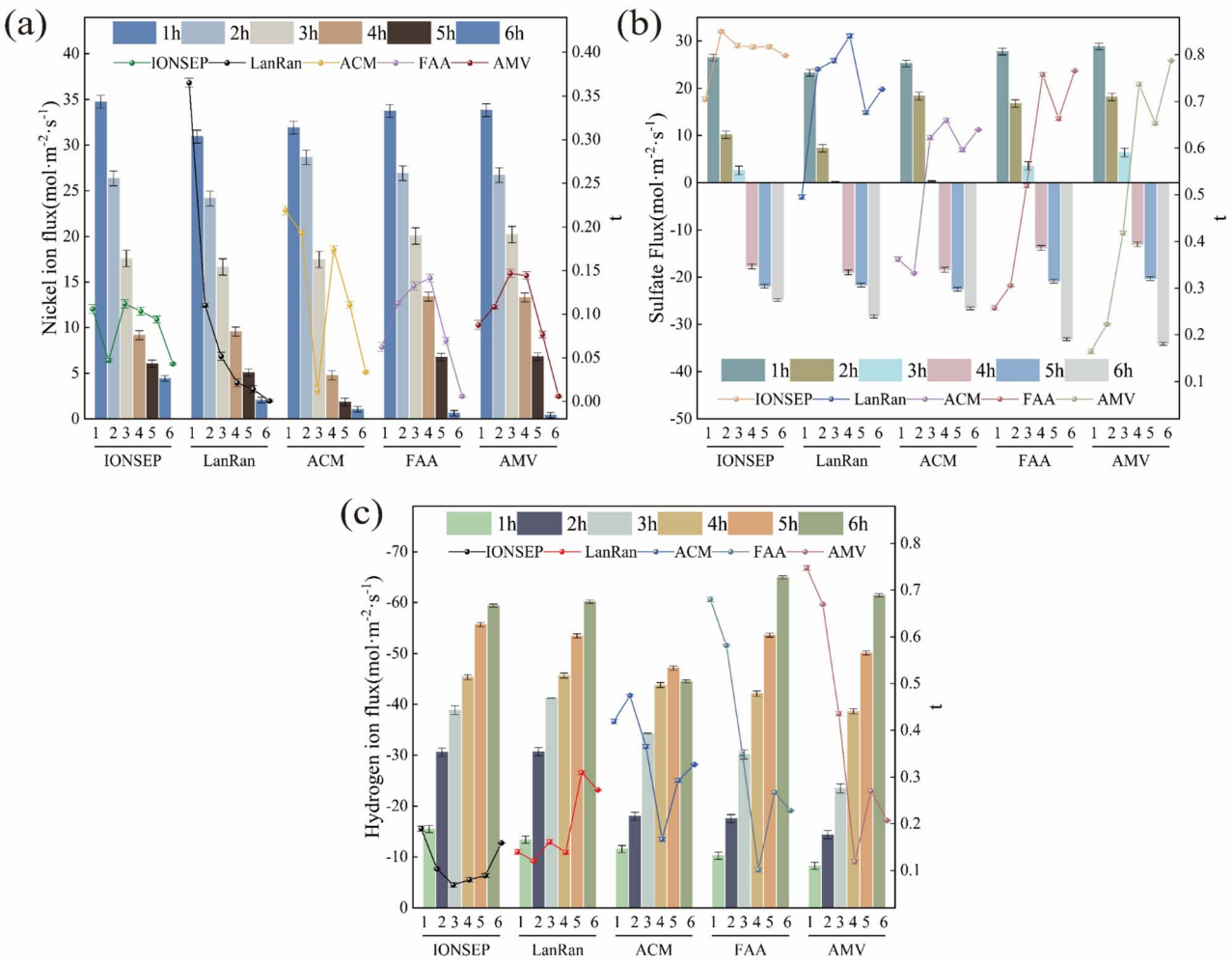

Fig. 12 (a) Variation in Ni^{2+} flux and migration number; (b) variation in SO_4^{2-} flux and migration number; (c) variation in H^+ flux and migration number.

where J_i is the ion flux (mol m^{-2} s^{-1}); Δc_i is the ion concentration difference between anode and cathode chambers (mol m^{-3}); t_i is the transference number or migration number of ion i, representing the fraction of current carried by that ion; D_i is the diffusion coefficient (m^2 s^{-1}), c_i is the ion concentration; δ_m is the membrane thickness (m); F is the Faraday's constant (96 485 C mol^{-1}); v is the fluid velocity (m s^{-1}).

Variations in the transference numbers reflect the relative contribution of each ion to total ionic transport. The most direct and accurate method for quantifying ion migration is the Hittorf method, which involves chemical analysis of different electrolyte regions after a known charge has passed through the system:[58]

$$t_i = \frac{z_i F \Delta n_i}{Q} \quad (10)$$

where t_i represents the transference number (or migration number) of ion i; Δn_i is the ion molarity difference between the anode and cathode chambers (mol); z_i is the ion charge; Q is the total charge (C); F is the Faraday's constant.

Fig. 12 illustrates the variation in ion fluxes during electrolysis. It can be seen that the Ni^{2+} flux decreases with the increase in electrolysis time. This decline is primarily ascribed to the depletion of Ni^{2+} within the concentration boundary layer at the cathode surface, which reduces the diffusion driving force. Concurrently, the rising cathode polarization overpotential further impedes the electrochemical reduction kinetics of Ni^{2+}. By contrast, the H^+ flux exhibits an upward trend as electrolysis progresses. This originates from the continuous OER at the anode, which generates a substantial amount of H^+. Under an applied electric field, this promotes partial transmembrane migration of H^+. Since the AEM does not completely block cations, some H^+ leakage is observed, resulting in non-equilibrium conditions. The SO_4^{2-} flux is initially positive, reflecting its migration from the cathode to the anode under the applied electric field. However, as electrolysis progresses, the flux gradually decreases. After approximately 4 h, the flux becomes negative, indicating intensified concentration polarization, a significant depletion of SO_4^{2-} in the cathode chamber, and the onset of reverse diffusion. This behavior is likely associated with variations in the concentration boundary layer at the membrane surface and increased migration resistance of hydrated ions.[59–61]

The migration number of SO_4^{2-} consistently dominates, reflecting the high selectivity of AEMs for anions, primarily due to the Donnan repulsion effect and the presence of fixed positive charge groups.[62] As electrolysis proceeds, the increased migration number of Ni^{2+} facilitates uniform metal deposition, consistent with the optimal electrolysis duration discussed in Section 3.1 and the characterization results in Section 3.2. The subsequent decrease in the Ni^{2+} migration number is associated with its declining concentration and reduced competitive migration.[63]

The rise in the H^+ migration number is attributed to its generation and accumulation in the anode chamber, as well as the protonation effects within the membrane transport channels. This process is regulated by the double-layer structure at the membrane–liquid interface, the fixed charge density within the membrane, and the electrolyte concentration gradient. Overall, concentration polarization not only modulates ion flux magnitudes but also redistributes migration numbers by relaxing local electroneutrality conditions. Ultimately, these effects determine both the nickel deposition efficiency and the acid recovery performance at the anode.[64,65]

4. Conclusions

This study systematically explored the application of single-membrane, dual-chamber electrolysis for nickel electrodeposition and sulfuric acid recovery. The optimal electrolysis duration was identified as 4 h, providing a balance between current efficiency, energy consumption, and sulfuric acid recovery. Among the tested AEMs, the AMV membrane demonstrated superior performance, achieving a cathodic current efficiency of 98.5%, sulfuric acid recovery concentration of 38.1 g L^{-1}, and relatively low energy consumption of 5945.8 kWh per tonne. These results highlight the exceptional electrochemical properties of the AMV membrane. Morphological and structural characterization confirmed the high quality of nickel deposits obtained under AMV conditions. SEM analysis revealed smooth, dense, defect-free deposits with continuous and uniform grain growth, while XRD analysis indicated a strong preferential grain growth orientation along the (220) plane, contributing to high crystallinity and purity of the nickel coating.

The observed ion transport behavior indicates that the proposed system enables simultaneous recovery of metallic nickel and sulfuric acid through the synergistic interplay between selective ion transport across AEMs and the electric-field-driven concentration gradients. This mechanism facilitates cathodic deposition of Ni^{2+} and SO_4^{2-} enrichment in the anode chamber, substantially enhancing resource utilization efficiency. Overall, the proposed single-membrane, dual-chamber electrolysis technology offers a practical and sustainable approach for nickel recovery and treatment of high-concentration nickel-containing wastewater.

Author contributions

Qiaoling Xian: conceptualization, data curation, methodology, writing – original draft. Jian Zhou: methodology, investigation, writing – original draft, writing – review and editing. Hongyi Liu: visualization, writing – review and editing. Chao Guo: formal analysis, writing – review and editing. Yan Lu: data curation, resources, validation. Xinyang Zhou: data curation, resources, validation.

Conflicts of interest

There are no conflicts of interest to declare.

Data availability

All the data supporting this article is included within the manuscript.

Acknowledgements

This research is supported by the National Natural Science Foundation of China (no. 52364055) and the Industry Support Program of University of Gansu Province (no. 2024CYZC-26).

References

1 K. Zhao, F. Gao and Q. Yang, *J. Sustain. Metall.*, 2022, **8**, 37–50.
2 Z. Xiao, P. Liu, L. Song, Z. Cao, J. Du, C. Zhou and P. Jiang, *Ionics*, 2021, **27**, 3207–3217.
3 Ihsanullah, A. Abbas, A. M. Al-Amer, T. Laoui, M. J. Al-Marri, M. S. Nasser, M. Khraisheh and M. A. Atieh, *Sep. Purif. Technol.*, 2016, **157**, 141–161.
4 W. Begum, S. Rai, S. Banerjee, S. Bhattacharjee, M. H. Mondal, A. Bhattarai and B. Saha, *RSC Adv.*, 2022, **12**, 9139–9153.
5 W. Guan, B. Zhang, S. Tian and X. Zhao, *Appl. Catal., B*, 2018, **227**, 252–257.
6 J. Ou, J. Yan, T. Xu, Z. Jiang, H. Tan, S. He, B. Hu and G. Yu, *J. Mol. Liq.*, 2021, **335**, 116246.
7 M. Akram, Z. Bano, S. U. A. Bhutto, J. Pan, A. Uddin, M. Z. Afzal, L. Li, M. Xia and F. Wang, *J. Environ. Chem. Eng.*, 2024, **12**, 112830.
8 H. Hase, T. Nishiuchi, T. Sato, T. Otake, T. Yaita, T. Kobayashi and T. Yoneda, *J. Hazard. Mater.*, 2017, **329**, 49–56.
9 M. Harahap, M. S. Abfertiawan and M. Syafila, *Jurnal Presipitasi: Media Komunikasi dan Pengembangan Teknik Lingkungan*, 2024, **21**, 300–323.
10 R. N. Raja Sulaiman and N. Othman, *Chem. Eng. Process.*, 2018, **134**, 9–19.
11 L. Song, J. Du, Z. Xiao, P. Jiang, Z. Cao and H. Zhu, *Front. Chem.*, 2020, **8**, 761.
12 I. Kruszelnicka, D. Ginter-Kramarczyk, W. Góra, K. Staszak, M. Baraniak, G. Lota and M. Regel-Rosocka, *Chem. Process Eng.*, 2022, **43**, 437–448.
13 N. A. A. Qasem, R. H. Mohammed and D. U. Lawal, *npj Clean Water*, 2021, **4**, 36.
14 R. N. R. Sulaiman and N. Othman, *J. Hazard. Mater.*, 2017, **340**, 77–84.
15 K. Kim, D. Raymond, R. Candeago and X. Su, *Nat. Commun.*, 2021, **12**, 6554.
16 E. Noman, A. Al-Gheethi, R. M. Saphira Radin Mohamed, M. Al-Sahari, M. S. Hossain, D.-V. N. Vo and M. Naushad, *Chemosphere*, 2022, **291**, 132862.
17 F. Wang, F. Liu, R. Elliott, S. Rezaei, L. T. Khajavi and M. Barati, *J. Alloys Compd.*, 2020, **822**, 153582.
18 N. Abdullah, N. Yusof, W. J. Lau, J. Jaafar and A. F. Ismail, *J. Ind. Eng. Chem.*, 2019, **76**, 17–38.
19 S. Tamersit, C. Amrane, A. Lalmi and I. Akkari, *Sep. Sci. Technol.*, 2024, **59**, 494–504.
20 P. Priyadarshi, K. Kishore and R. Maurya, *Int. J. Interact. Des. Manuf.*, 2023, **17**, 1489–1495.
21 G. S. Tsurtsumia, N. S. Koiava, N. S. Gogishvili, I. T. Zaridze, I. B. Kakhniashvili, G. G. Gorelishvili, V. M. Kveselava and P. N. Nikoleishvili, *J. Electrochem. Soc.*, 2015, **162**, E96.
22 M. M. Kamel and A. M. Bastaweesy, *Water, Air, Soil Pollut.*, 2024, **235**, 480.
23 J. Lu, Q. Yang and Z. Zhang, *Trans. Nonferrous Met. Soc. China*, 2010, **20**, s97–s101.
24 X. Ren, Q. Wei, S. Hu and S. Wei, *J. Hazard. Mater.*, 2010, **181**, 908–915.
25 R. S. Kingsbury, S. Flotron, S. Zhu, D. F. Call and O. Coronell, *Environ. Sci. Technol.*, 2018, **52**, 4929–4936.
26 J. Ayach, W. El Malti, L. Duma, J. Lalevée, M. Al Ajami, H. Hamad and A. Hijazi, *Polymers*, 2024, **16**, 1959.
27 F. Rögener, M. Sartor, A. Bán, D. Buchloh and T. Reichardt, *Resour., Conserv. Recycl.*, 2012, **60**, 72–77.
28 S. Loza, N. Loza, N. Kovalchuk, N. Romanyuk and J. Loza, *Membranes*, 2023, **13**, 396.
29 K. Yan, P. Huang, M. Xia, X. Xie, L. Sun, W. Lei and F. Wang, *Sep. Purif. Technol.*, 2022, **295**, 121283.
30 X. Song, Q. Shen, B. Liu, J. Li and D. Zhu, *Electrochemistry*, 2024, **92**, 077004.
31 Y. He, F. Ding, L. Lin, Z. Wang and Y. Zhang, *Acta Phys.-Chim. Sin.*, 2020, 2009001.
32 R. Sim and A. Manthiram, *Adv. Energy Mater.*, 2024, **14**, 2303985.
33 H. Ito, N. Kawaguchi, S. Someya, T. Munakata, N. Miyazaki, M. Ishida and A. Nakano, *Int. J. Hydrogen Energy*, 2018, **43**, 17030–17039.
34 L. Bao, Z. Xu, W. Guo, S. Lin and S. Sun, *Colloids Surf., A*, 2023, **674**, 131884.
35 J. Zhou, S. F. Wang and X. S. Song, *Trans. Nonferrous Met. Soc. China*, 2016, **26**, 1706–1713.
36 Y. Chen, H. Yang, H. Feng, P. Yang, J. Zhang and B. Shu, *Mater. Today Commun.*, 2023, **35**, 106058.
37 Y. Xu, K. Huang, Z. Zhu and T. Xia, *Surf. Coat. Technol.*, 2019, **370**, 1–10.
38 L. N. Furini, C. S. Martin, S. A. Camacho, R. J. G. Rubira, J. D. Fernandes, E. A. Silva, T. C. Gomes, G. M. Stunges, C. J. L. Constantino and P. Alessio, *Thin Solid Films*, 2020, **699**, 137897.
39 R. Pérez-Garibay, J. C. Rojas-Montes, S. Bello-Teodoro and J. M. Flores-Álvarez, *J. Appl. Electrochem.*, 2020, **50**, 1291–1299.
40 M. Kawaguchi and H. Hamada, *J. Nucl. Sci. Technol.*, 2014, **51**, 201–207.
41 B. Mallory and K. Parker, *Plat. Surf. Finish.*, 1991, 55–58.
42 N. Miao, J. Jiang and W. Wu, *J. Nanomater.*, 2018, 1817542.
43 S. Deabate, F. Fourgeot and F. Henn, *J. Power Sources*, 2000, **87**, 125–136.
44 E. P. S. Schmitz, S. P. Quinaia, J. R. Garcia, C. K. De Andrade and M. C. Lopes, *Int. J. Electrochem. Sci.*, 2016, **11**, 983–997.
45 J. Deng, K. Li, J. Fu, B. Li, H. Jiang, H. Ju, E. Wang, C. Zhang, Y. Liu, Y. Chen, F. Wu and C. Su, *Coatings*, 2023, **13**, 1519.
46 A. M. Alfantazi and A. Shakshouki, *J. Electrochem. Soc.*, 2002, **149**, C506.
47 J. R. Hernández-Tapia, J. Vazquez-Arenas and I. González, *Electrochim. Acta*, 2013, **103**, 266–274.

48 A. Campione, A. Cipollina, I. D. L. Bogle, L. Gurreri and G. Micale, *Desalination*, 2019, **465**, 79–93.
49 X. Ren, Q. Wei, Z. Liu and J. Liu, *Trans. Nonferrous Met. Soc. China*, 2012, **22**, 467–475.
50 J. Gao, H. Zhang, X. Zhao, Y. Wang, H. Zhu, X. Kong, Y. Liang, T. Ou, R. Ren, Y. Gu, Y. Su and J. Zhang, *Chin. J. Struct. Chem.*, 2025, **44**, 100563.
51 A. Habrioux, C. Morais, T. W. Napporn and B. Kokoh, *Curr. Opin. Electrochem.*, 2020, **21**, 146–159.
52 A. Graff, E. Barrez, P. Baranek, M. Bachet and P. Bénézeth, *J. Solution Chem.*, 2017, **46**, 25–43.
53 H. Strathmann, *Desalination*, 2010, **264**, 268–288.
54 F. Wei, A. Kosakian, J. Liu, J. Kracher, R. Khan and M. Secanell, *J. Power Sources*, 2023, **557**, 232494.
55 L. Liu and Q. Cheng, *Renewable Sustainable Energy Rev.*, 2020, **134**, 110115.
56 Z. Zourmand, F. Faridirad, N. Kasiri and T. Mohammadi, *Desalination*, 2015, **359**, 41–51.
57 Y. Tanaka, in *Ion Exchange Membranes: Fundamentals and Applications*, 2015, pp. 29–65.
58 K. Xu, *Commun. Mater.*, 2022, **3**, 31.
59 C. Fang, A. Mistry, V. Srinivasan, N. P. Balsara and R. Wang, *JACS Au*, 2023, **3**, 306–315.
60 B. Balu and A. S. Khair, *Soft Matter*, 2018, **14**, 8267–8275.
61 J. Liu, Y. Zhao, R. Gao, L. Zhang, X. Jiang, Y. Miao, S. Cheng, G. Dong and T. Zhang, *Sep. Purif. Technol.*, 2025, **358**, 130141.
62 D. Asante-Sackey, S. Rathilal, E. Kweinor Tetteh, E. O. Ezugbe and L. V. Pillay, *Membranes*, 2021, **11**, 358.
63 J. Si, X. Li, N. Ren, H. He, S. Zeng and C. Chen, *J. Power Sources*, 2024, **599**, 234225.
64 É. Lucas, L. Han, I. Sullivan, H. A. Atwater and C. Xiang, *Front. Energy Res.*, 2022, **10**, 1001684.
65 H. He, Q. Chen, R. Fu, Z. Liu, L. Ge and T. Xu, *Chem Bio Eng.*, 2024, **1**, 647–657.